ACADEMIC PRESS

Available online at www.sciencedirect.com

SCIENCE DIRECT®

Journal of Sound and Vibration 265 (2003) 967–985

JOURNAL OF SOUND AND VIBRATION

www.elsevier.com/locate/jsvi

Acoustic behavior of circular dual-chamber mufflers

A. Selamet[a,*], F.D. Denia[b], A.J. Besa[b]

[a] *Department of Mechanical Engineering and The Center for Automotive Research, The Ohio State University, Columbus, OH 43210-1107, USA*

[b] *Departamento de Ingeniería Mecánica y de Materiales, Universidad Politécnica de Valencia, Camino de Vera s/n, 46022 Valencia, Spain*

Received 20 June 2001; accepted 18 August 2002

Abstract

The acoustic behavior of a circular dual-chamber muffler is investigated in detail by: (1) a two-dimensional (2-D) axisymmetric analytical approach based on the mode-matching technique for the concentric configurations; (2) the finite element method; and (3) experimental work. A number of effects is studied, including (1) the presence of a rigid baffle in the chamber; (2) the inner radius of the baffle; (3) the position of the baffle along the axial direction; and (4) the extended inlet/outlet and baffle ducts. Some of these effects are shown to modify the acoustic behavior drastically, suggesting potential means to improve the acoustic performance.

1. Introduction

The presence of a partition in an expansion chamber is known, through a planar wave propagation model, to lead to a wider-dome acoustic attenuation behavior with reduced number of pass-bands and increased transmission loss (TL) [1]. In order to capture primarily the non-planar propagation and attenuation in these configurations, the present work develops a two-dimensional axisymmetric analytical solution of the wave equation based on mode matching. This technique has been shown to be effective when the eigenfunctions of the geometry are simple to obtain, such as rectangular, circular, and elliptical ducts [2–6]. The influence of the area ratio [1], chamber length [7], inlet/outlet locations [8,9], and duct extensions [10] have been studied in detail for circular single-chamber mufflers. The acoustic attenuation of dual-chamber mufflers is also expected to depend on these geometric characteristics, as well as on the presence of the baffle, the

*Corresponding author. Tel.: +1-614-292-4143; fax: +1-614-292-3163.
E-mail address: selamet.1@osu.edu (A. Selamet).

0022-460X/03/$ - see front matter
doi:10.1016/S0022-460X(02)01258-0

radius of the baffle hole, the position of the baffle along the axis of the chamber, and the presence of extended ducts in the partition. In an abstract [11], Xiao and Prasad indicated that they obtained the insertion loss of baffle-simple expansion chamber by using the boundary element method and experiments. The hole radius and the position of the baffle were shown to have a significant effect on the attenuation.

The objective of the present work is to investigate the acoustic performance of dual-chamber configurations in detail primarily by an analytical approach. Finite element calculations [12] and experimental results for a selected configuration based on a two-microphone technique [13] are included for comparison with the analytical results. The one-dimensional (1-D) propagation model is also used to illustrate the discrepancies with respect to the multi-dimensional results, even at low frequencies, due to the presence of evanescent higher order modes in the baffle hole, thereby establishing the need for length corrections [14–16] in the 1-D model.

Following this Introduction, Section 2 describes the 2-D axisymmetric analytical approach developed by using the continuity of the acoustic pressure and axial velocity at the area changes, and the orthogonality properties of the Bessel functions. Section 3 applies the technique to a number of configurations to analyze the foregoing effects, and compares the analytical results with those from finite element method (FEM) and experiments. The study is concluded in Section 4 with final remarks.

2. Analytical approach

Fig. 1 shows the geometry of a circular dual-chamber muffler considered in this study. The Helmholtz equation [1],

$$\nabla^2 P + k^2 P = 0, \tag{1}$$

governs the linearized acoustics inside such a configuration, with P being the acoustic pressure and $k = \omega/c_0$ the wave number (ω the angular frequency and c_0 the speed of sound). The solution of Eq. (1) may be written, for a circular, concentric and rigid duct, as [10]

$$P(r, z_1) = \sum_{n=0}^{\infty} (A_n^+ \mathrm{e}^{-\mathrm{j}k_{A,n}z_1} + A_n^- \mathrm{e}^{\mathrm{j}k_{A,n}z_1})\psi_{A,n}(r) = \sum_{n=0}^{\infty} (A_n^+ \mathrm{e}^{-\mathrm{j}k_{A,n}z_1} + A_n^- \mathrm{e}^{\mathrm{j}k_{A,n}z_1})\mathrm{J}_0\left(\alpha_n \frac{r}{R_1}\right), \tag{2}$$

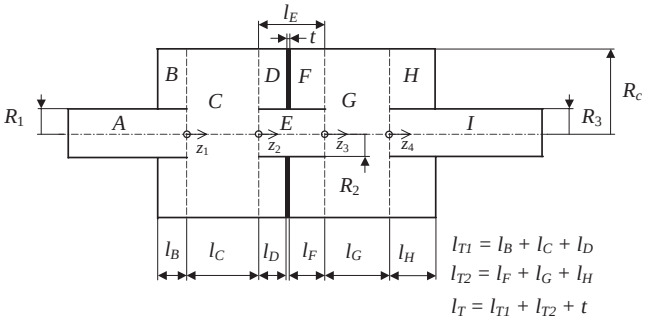

Fig. 1. Circular dual-chamber muffler.

where $j = \sqrt{-1}$ is the imaginary unit, n the mode number, (r, z_1) the cylindrical co-ordinates, A_n^+ and A_n^- the wave propagation coefficients, $\psi_{A,n}(r)$ the eigenfunction (which is given by $J_0(\alpha_n r/R_1)$, the Bessel function of the first kind and order 0), and α_n the eigenvalue satisfying the rigid wall boundary condition. The axial wave number of the mode n is given by

$$k_{A,n} = \sqrt{k^2 - \left(\frac{\alpha_n}{R_1}\right)^2}. \tag{3}$$

In the case of an annular duct, the solution of the Helmholtz equation (1) yields [10]

$$\begin{aligned} P(r, z_1) &= \sum_{n=0}^{\infty} (B_n^+ e^{-jk_{B,n}z_1} + B_n^- e^{jk_{B,n}z_1})\psi_{B,n}(r) \\ &= \sum_{n=0}^{\infty} (B_n^+ e^{-jk_{B,n}z_1} + B_n^- e^{jk_{B,n}z_1})\left(J_0\left(\beta_{B,n}\frac{r}{R_C}\right) - \frac{J_1(\beta_{B,n})}{Y_1(\beta_{B,n})}Y_0\left(\beta_{B,n}\frac{r}{R_C}\right)\right), \end{aligned} \tag{4}$$

B_n^+ and B_n^- being the wave propagation coefficients and $\psi_{B,n}(r)$ the eigenfunction given by

$$J_0\left(\beta_{B,n}\frac{r}{R_C}\right) - \frac{J_1(\beta_{B,n})}{Y_1(\beta_{B,n})}Y_0\left(\beta_{B,n}\frac{r}{R_C}\right). \tag{5}$$

Here, J_1 is the Bessel function of the first kind and order 1, Y_0 and Y_1 are the Bessel functions of the second kind and order 0 and 1, respectively, and $\beta_{B,n}$ is the eigenvalue satisfying the rigid wall boundary condition in the inner and outer annulus walls. The axial wave number can be obtained by means of

$$k_{B,n} = \sqrt{k^2 - \left(\frac{\beta_{B,n}}{R_C}\right)^2}. \tag{6}$$

The continuity conditions at the first expansion are

$$P_A|_{z_1=0} = P_C|_{z_1=0} \quad \text{on } S_A, \tag{7}$$

$$U_A|_{z_1=0} = U_C|_{z_1=0} \quad \text{on } S_A, \tag{8}$$

$$P_B|_{z_1=0} = P_C|_{z_1=0} \quad \text{on } S_B, \tag{9}$$

$$U_B|_{z_1=0} = U_C|_{z_1=0} \quad \text{on } S_B, \tag{10}$$

where U denotes the axial acoustic velocity, given by the momentum equation $j\rho_0\omega U = -\partial P/\partial z$ (ρ_0 being the fluid density). At the first contraction, the continuity conditions yield

$$P_C|_{z_1=l_C} = P_E|_{z_2=0} \quad \text{on } S_E, \tag{11}$$

$$U_C|_{z_1=l_C} = U_E|_{z_2=0} \quad \text{on } S_E, \tag{12}$$

$$P_C|_{z_1=l_C} = P_D|_{z_2=0} \quad \text{on } S_D, \tag{13}$$

$$U_C|_{z_1=l_C} = U_D|_{z_2=0} \quad \text{on } S_D. \tag{14}$$

Similar equations are considered for the second expansion,

$$P_E|_{z_2=l_E} = P_G|_{z_3=0} \quad \text{on } S_E, \tag{15}$$

$$U_E|_{z_2=l_E} = U_G|_{z_3=0} \quad \text{on } S_E, \tag{16}$$

$$P_F|_{z_3=0} = P_G|_{z_3=0} \quad \text{on } S_F, \tag{17}$$

$$U_F|_{z_3=0} = U_G|_{z_3=0} \quad \text{on } S_F \tag{18}$$

and, for the second contraction,

$$P_G|_{z_3=l_G} = P_1|_{z_4=0} \quad \text{on } S_I, \tag{19}$$

$$U_G|_{z_3=l_G} = U_1|_{z_4=0}, \quad \text{on } S_I, \tag{20}$$

$$P_G|_{z_3=l_G} = P_H|_{z_4=0} \quad \text{on } S_H, \tag{21}$$

$$U_G|_{z_3=l_G} = U_H|_{z_4=0} \quad \text{on } S_H. \tag{22}$$

Finally, the rigid plate boundary conditions are expressed. At the left wall,

$$U_B|_{z_1=-l_B} = 0 \quad \text{on } S_B, \tag{23}$$

which leads to Eq. (8) in Ref. [10], with subscript 1 being replaced by B. The rigid plate boundary condition at the central wall (left side),

$$U_D|_{z_2=l_D} = 0 \quad \text{on } S_D, \tag{24}$$

gives Eq. (17) of Ref. [10] by substituting 2 by D. At the right side of the central wall

$$U_F|_{z_3=-l_F} = 0 \quad \text{on } S_F, \tag{25}$$

thus

$$F_n^+ = F_n^- \mathrm{e}^{-2\mathrm{j}k_{F,n}l_F}. \tag{26}$$

At the right wall of the chamber

$$U_H|_{z_4=l_H} = 0 \quad \text{on } S_H, \tag{27}$$

which leads to

$$H_n^- = H_n^+ \mathrm{e}^{-2\mathrm{j}k_{H,n}l_H}. \tag{28}$$

To obtain an algebraic system from Eqs. (7)–(22), the orthogonality properties of the eigenfunctions are used as shown in Ref. [10]. The first expansion and the first contraction are considered, leading to Eqs. (13)–(15) and (22)–(24) in Ref. [10], where l_B is equivalent to l_1 in Eqs. (14) and (15), and l_D is equivalent to l_2 in Eqs. (23) and (24) of Ref. [10].

For the second expansion and the second contraction of the chamber, the same procedure leads to a similar set of equations, as illustrated next. Eq. (15) becomes

$$(E_s^+ e^{-jk_{E,s}l_E} + E_s^- e^{jk_{E,s}l_E})\langle \psi_{E,s}\psi_{E,s}\rangle_{S_E} = \sum_{n=0}^{\infty}(G_n^+ + G_n^-)\langle \psi_{G,n}\psi_{E,s}\rangle_{S_E}, \tag{29}$$

$\langle\,\rangle_S$ being the integration over S. Eq. (17) yields Eq. (14) in Ref. [10] by replacing coefficients B and C by F and G, respectively, and length l_1 by l_F. Eqs. (16) and (18) lead to

$$\sum_{n=0}^{\infty} k_{E,n}(E_n^+ e^{-jk_{E,n}l_E} - E_n^- e^{jk_{E,n}l_E})\langle \psi_{E,n}\psi_{G,s}\rangle_{S_E} + \sum_{n=0}^{\infty} k_{F,n}F_n^-(e^{-2jk_{F,n}l_F} - 1)\langle \psi_{F,n}\psi_{G,s}\rangle_{S_F}$$
$$= k_{G,s}(G_s^+ - G_s^-)\langle \psi_{G,s}\psi_{G,s}\rangle_{S_G}. \tag{30}$$

For the second contraction, Eqs. (19)–(22) may be expressed as Eqs. (22)–(24) of Ref. [10], after substitution of coefficients C by G, E by I and D by H. In addition, lengths l_C and l_2 are replaced by l_G and l_H, respectively.

To evaluate the integrals of the eigenfunctions, the expressions in Appendix A are used. The truncation of the previous system of equations allows the calculation of the propagation coefficients, and therefore the TL of the dual-chamber muffler. Details of the procedure can be found elsewhere [7].

3. Results and discussion

For most of the configurations considered in the analytical and computational parts of the study, the radii of the chamber and the inlet/outlet ducts are similar to those used in Ref. [10], that is, $R_C = 0.0766$ m and $R_1 = R_3 = 0.0243$ m. A baffle is now added with a thickness $t = 0.001$ m. The total chamber length l_T and the rest of dimensions considered in each particular configuration are included in Table 1. These dimensions are chosen to study different effects including the partition, the baffle hole radius, the axial baffle location, and the presence of extended ducts. The dimensions of the configuration selected to perform the experiment differ slightly from those aforementioned, and will be specified later in Section 3.4.

Table 1
Dual-chamber muffler geometry ($R_C = 0.0766$ m and $R_1 = R_3 = 0.0243$ m)

Effect		Geometry	Total length l_T (m)	Hole radius R_2 (m)
Partition		1	0.28	0.0243
	Baffle position	2	0.40	0.0243
Hole radius		3	0.28	0.0175
		4	0.28	0.0375
		5	0.28	0.05
		6	0.40	0.0175
		7	0.40	0.0375
		8	0.40	0.05

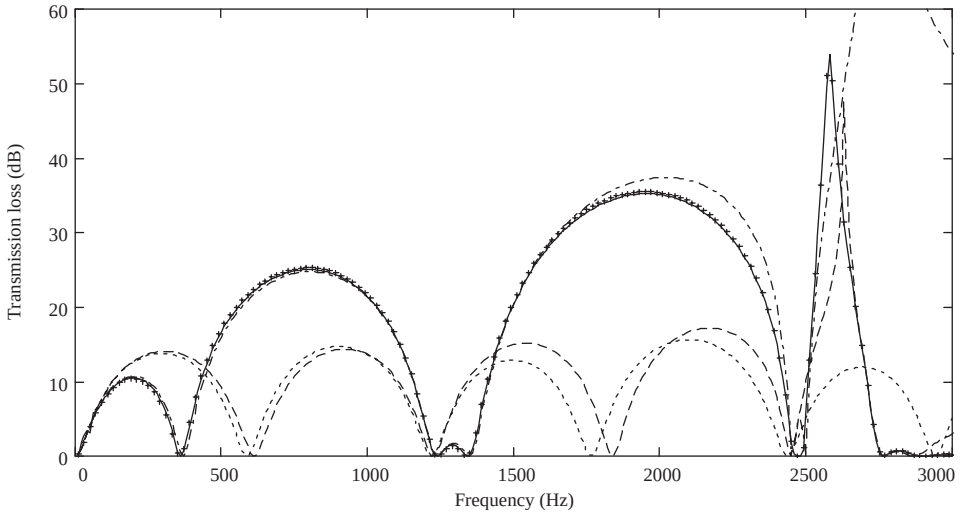

Fig. 2. Transmission loss of dual-chamber muffler with $l_T = 0.28$ m, geometry 1: ——, analytical; +, FEM; - - - -, plane wave model; – – – –, corrected plane wave model; – – –, analytical, simple expansion chamber without baffle.

3.1. Effect of the partition

First, the effect of the presence of a rigid baffle inside the chamber is analyzed with geometries 1 and 2 and $R_1 = R_2 = R_3$. The baffle is located axially at the center of the chamber. Fig. 2 shows, for the first chamber length $l_T = 0.28$ m, the TL obtained by the analytical approach and finite element calculations, which are shown to agree well. The frequency $f = \omega/(2\pi)$ will be used in the x-axis along this work. The transition from frequency to Helmholtz number kR_1 can be easily obtained by means of the scaling factor

$$kR_1 = 4.491 \times 10^{-4} f, \tag{31}$$

where the entrance pipe radius is $R_1 = 0.0243$ m and a value $c_0 = 340$ m/s is used in the calculations.

A simple expansion chamber without baffle is included for comparison purposes, whose TL has been calculated by means of the mode-matching method [7]. In addition, the 1-D model is considered for the dual-chamber muffler (see Appendix B for details). The approximate end corrections δ_{inlet} and δ_{outlet} given by [15]

$$\delta_{inlet} = \frac{8\rho_0 S_A H(R_1/R_C, kR_C)}{3\pi^2 R_1}, \tag{32}$$

$$\delta_{outlet} = \frac{8\rho_0 S_I H(R_3/R_C, kR_C)}{3\pi^2 R_3} \tag{33}$$

are used for the inlet and outlet ducts, respectively, H being the Karal correction factor. A length correction

$$\delta_{baffle} = R_2(0.44544 + 0.049955\, kR_2 + 0.022517(kR_2)^2 + 0.083479(kR_2)^3) \tag{34}$$

is applied to both sides of the baffle hole, which is based on Table 3 of Appendix B (for $R_2 = 0.0243$ m). These corrections take into account the excitation of higher order modes at the area discontinuities.

Fig. 2 exhibits a dome-like behavior for the dual-chamber muffler, as expected. The nearly equal pair of domes of expansion chamber without baffle is now replaced by unequal pairs: the first dome of each pair is smaller in amplitude and frequency band than the second one. When the frequency increases, the first dome of the pair tends to disappear, the second dome widens and tends to cover the two domes of the simple expansion chamber. Such broadband behavior disappears when the higher order modes start to propagate, the cut-off frequency being 2705 Hz. The 1-D model without end corrections fails at considerably low frequencies while exhibiting a TL close to that of a simple expansion chamber without baffle. The generation of evanescent higher order modes through the central plate is not considered in the 1-D model, and thus the behavior is similar to the simple expansion chamber. The corrected plane wave model improves the prediction considerably as the results become acceptable up to 2500 Hz. The undesirable deterioration of the TL at low frequencies for the dual-chamber muffler in comparison with the single expansion chamber without baffle is associated with the generation of evanescent higher order modes at the baffle hole, which produce a pass-band at 360 Hz.

A similar discussion follows for Fig. 3, which considers geometry 2. Since the chamber length is increased, the number of domes is also higher, as expected. The multi-dimensional results for the dual-chamber configuration are similar, and important discrepancies are found in comparison with the plane wave model without correction. The peak acoustic attenuation performance of the dual chamber is improved with increasing frequency in all cases in comparison with the simple expansion chamber. Since the first dome of each pair almost disappears and the second one tends to cover two domes of the simple expansion configuration, a broader attenuation band is obtained

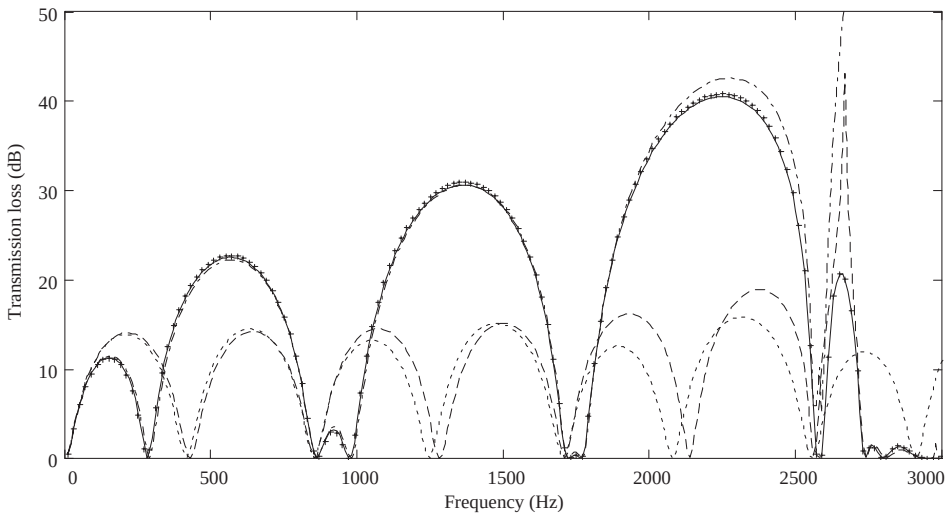

Fig. 3. Transmission loss of dual-chamber muffler with $l_T = 0.40$ m, geometry 2: ——, analytical; +, FEM; - - - -, plane wave model; – – – –, corrected plane wave model; – – –, analytical, simple expansion chamber without baffle.

Table 2
Behavior of the dual-chamber muffler between the last well-defined dome and the onset of higher order mode propagation

Total chamber length l_T (m)	Number of domes. Simple expansion chamber	Behavior	Number of wide domes. Dual-chamber muffler	Behavior
0.28	4	Peak	2	Peak
0.34	5	Narrow dome	2	Peak
0.40	6	Peak	3	Narrow dome
0.46	7	Narrow dome	3	Narrow dome
0.52	8	Peak	4	Peak
0.58	9	Narrow dome	4	Peak

in general. The amplitude is increased due to the presence of two expansions and two contractions in the same overall chamber.

Next, an aspect is elaborated in connection to the relation between the last well-defined dome and the onset of multi-dimensional propagation. For a simple expansion chamber, the TL for configurations with an even number of domes exhibits a sharp peak, but this peak does not appear in the cases with an odd number of domes, which yield a final narrow dome [7]. For dual-chamber mufflers, this behavior is also observed, but only the number of wide domes (or pairs of domes) needs to be considered. It can be shown that configurations with an even number of wide TL domes exhibit a peak before the higher order mode propagation, whereas those with an odd number of wide domes show a narrow dome. The results are summarized in Table 2, with some additional data obtained for several chamber lengths.

3.2. *Effect of the baffle hole radius*

The effect of hole radius is examined next, again with the baffle axially centered. Three different values of the radius and two total chamber lengths are considered, associated with the geometries 3–8. The results obtained from the analytical model and finite element calculations are depicted in Figs. 4 and 5, with total chamber lengths of $l_T = 0.28$ and 0.40 m, respectively. Both figures show good agreement among the multi-dimensional results. The transmission loss amplitude shows a general increase when the baffle hole radius is reduced, as expected. Also, in the limit of $R_2 = R_C$ the results would clearly approach those of a simple expansion chamber. As the hole radius becomes smaller, the first dome amplitude and frequency range are reduced.

The limitations of the plane wave model and the benefits of the end corrections are shown in Fig. 6, in which the analytical multi-dimensional solution is used as a reference for comparison. The chamber defined by geometry 3 is used, with hole radius $R_2 = 0.0175$ m. For the corrected plane wave model, the values δ_{inlet} and δ_{outlet} given by Eqs. (32) and (33) are used for the inlet and outlet, and the correction

$$\delta_{baffle} = R_2(0.539896 + 0.065188kR_2 + 0.11981(kR_2)^2 + 0.079608(kR_2)^3) \tag{35}$$

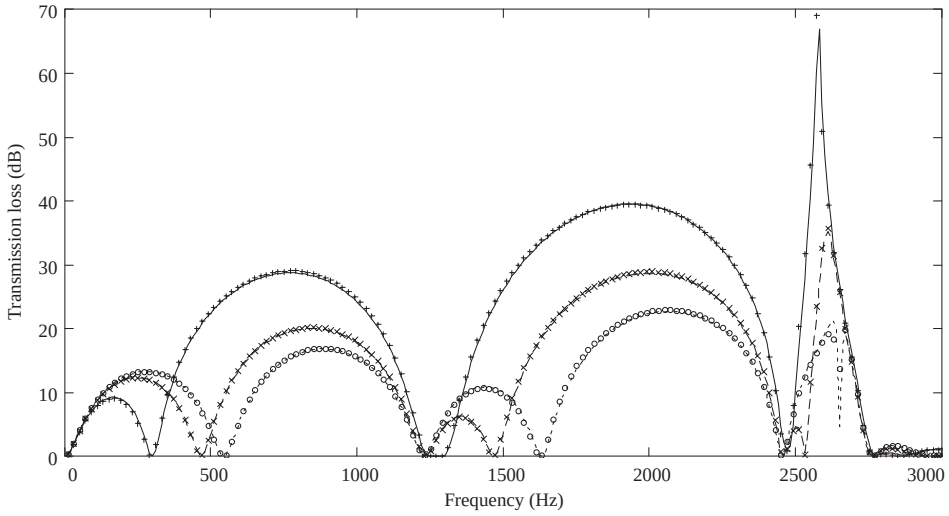

Fig. 4. Transmission loss of dual-chamber muffler with $l_T = 0.28$ m: ——, geometry 3, analytical; +, same, FEM; – – –, geometry 4, analytical; ×, same, FEM; - - - -, geometry 5, analytical; ○, same, FEM.

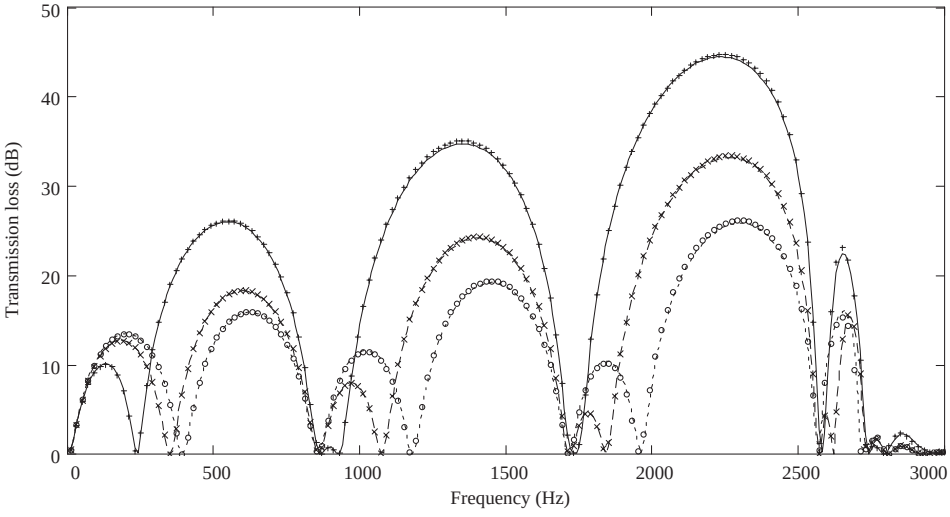

Fig. 5. Transmission loss of dual-chamber muffler with $l_T = 0.40$ m: ——, geometry 6, analytical; +, same, FEM; – – –, geometry 7, analytical; ×, same, FEM; - - - -, geometry 8, analytical; ○, same, FEM.

is applied to both sides of the baffle hole following Table 3 of Appendix B (for $R_2 = 0.0175$ m). With these end corrections, the 1-D prediction is able to reproduce the pass-band at 300 Hz, which appears to be a drawback in the acoustic attenuation performance of the dual-chamber muffler.

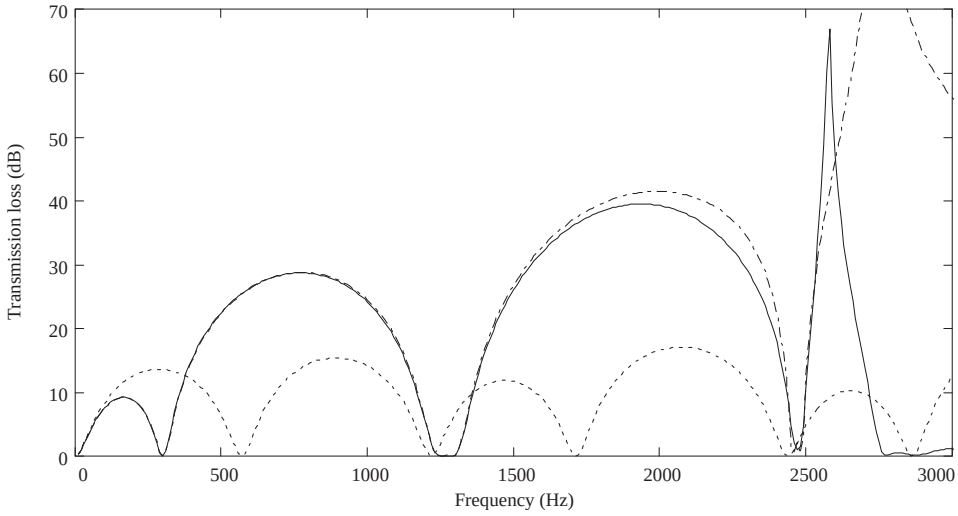

Fig. 6. Transmission loss of dual-chamber muffler, geometry 3: ——, analytical; - - - -, plane wave model without correction; – – – –, corrected plane wave model.

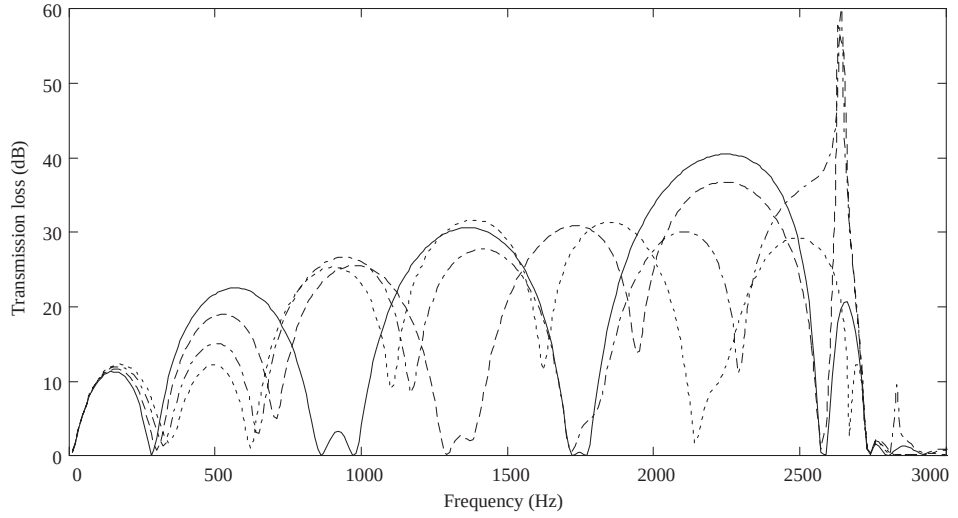

Fig. 7. Transmission loss of dual-chamber muffler, geometry 2: ——, centered baffle; – – –, $l_T/3$ baffle; – - – - $l_T/4$ baffle; - - - -, $l_T/5$ baffle.

3.3. *Effect of the baffle position*

The effect of the baffle position along the axis of the chamber on the acoustic behavior is examined here. In addition to the central position of earlier sections, the following distances from the inlet are considered for geometry 2: $l_T/3, l_T/4$ and $l_T/5$. The analytical results are depicted in Fig. 7.

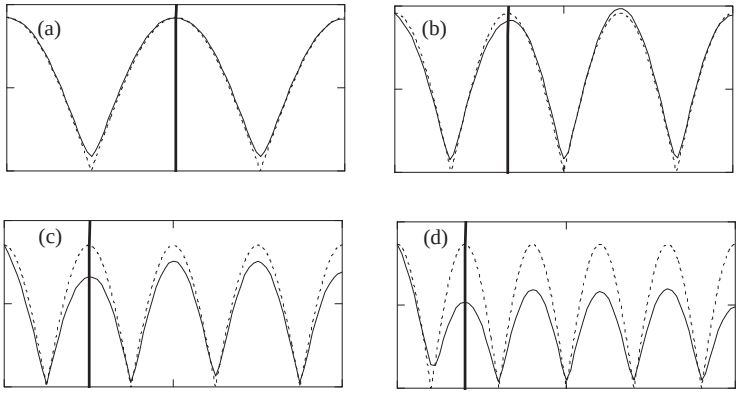

Fig. 8. Pressure amplitude along the axis of dual-chamber muffler, geometry 2: ----, 1-D closed cavity; ——, FEM. (a) centered baffle, 1-D with $f = 850$ Hz, FEM with $f = 861.7$ Hz. (b) $l_T/3$ baffle, 1-D with $f = 1275$ Hz, FEM with $f = 1291.5$ Hz. (c) $l_T/4$ baffle, 1-D with $f = 1700$ Hz, FEM with $f = 1718.6$ Hz. (d) $l_T/5$ baffle, 1-D with $f = 2125$ Hz, FEM with $f = 2143.35$ Hz.

The axial location of the baffle strongly affects the acoustic performance. The first attenuation dome is similar for all cases and the first pass-band increases slightly as the baffle is offset (from 280 to 350 Hz). The second dome has higher amplitude when the configuration is closer to the central baffle. The pass-band of the centered chamber at 861 Hz is moved to 1291 Hz for the $l_T/3$ configuration, to 1718 Hz for the $l_T/4$ chamber, and to 2143 Hz for the $l_T/5$ geometry. These frequencies can be evaluated approximately with the plane wave model, and, as expected, are higher as the baffle moves away from the center. For this pass-band, Fig. 8 shows the comparison of the 1-D model (closed cavity) and FEM for the pressure amplitude along the axis of the chamber. For the numerical computation, the inlet pipe is excited with a pressure amplitude of unity, the outlet has an anechoic termination, and both inlet and outlet lengths are 0.1 m. Fig. 8 shows the pressure only in the chamber (i.e., the inlet and outlet ducts are excluded) and a vertical thick line is included to show the position of the baffle. Also, the 1-D results have been scaled so that the pressure value on the left side of the chamber is equal to that given by FEM. The pressure lines predicted by the two models show similar trends. The same number of wavelengths is observed but the amplitude error increases for higher frequencies. The location of the pass-band can be controlled by moving the partition, which improves the acoustic performance of the chamber locally.

3.4. Extended ducts

Finally, the presence of extended ducts in the chamber is studied. As shown in Ref. [10], it is possible to obtain a general improvement in the acoustic attenuation of a simple expansion chamber by means of properly extended ducts. The pass-bands associated with the first axial modes can be removed including inlet/outlet ducts with extensions so that these resonate at the frequencies of the pass-bands. This can finally lead to a wide dome in the transmission loss up to the propagation of the higher order modes. The same behavior is also expected in the dual-chamber muffler, in which four ducts can be used with extensions. Fig. 9 compares the analytical

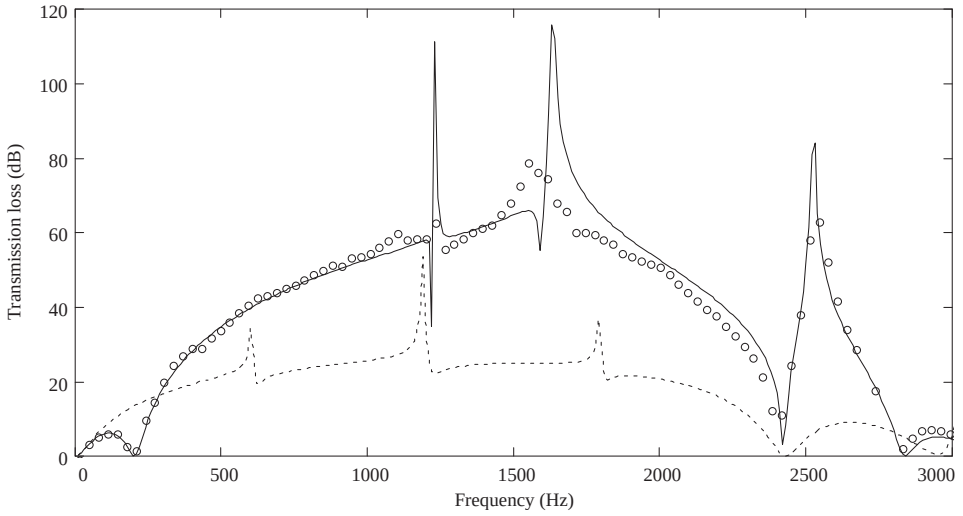

Fig. 9. Effect of duct extensions on the transmission loss: ----, simple expansion chamber, analytical; ——, dual-chamber muffler, analytical; ○, same, experimental.

results for TL of a simple expansion chamber and a centered dual-chamber muffler. Also included are the experimental results for the latter configuration. The dimensions of the partitioned configuration are $R_1 = R_2 = R_3 = 0.02464\,\text{m}$, $R_C = 0.07645\,\text{m}$, $l_T = 0.2823\,\text{m}$ and $t = 0.002286\,\text{m}$. The extended lengths are $l_B = l_F = 0.059\,\text{m}$ and $l_D = l_H = 0.025\,\text{m}$ for the dual-chamber muffler. For the simple expansion chamber, the same dimensions R_1, R_3, R_C and l_T are considered, with the extensions being $l_B = 0.131\,\text{m}$ and $l_H = 0.061\,\text{m}$ to retain a similarity to Ref. [10].

The agreement between the measurement and the analytical prediction is reasonable, while the small discrepancies may possibly be attributed to the neglected viscous effects and wall thickness in the analytical model. The dual-chamber muffler exhibits an amplitude increase (more than twice over a broad frequency range) in comparison with the simple expansion chamber, with the exception of frequencies close to the pass-band at 190 Hz. This deterioration of the dual-chamber muffler at low frequencies due to the presence of the baffle presents a challenge, and may be removed in a combination with, for example, a Helmholtz chamber tuned near this frequency. The improvement in the acoustic attenuation performance of the dual-chamber muffler from about 300 Hz up to 2400 Hz is evident, which is due to the combination of extended ducts and a number of area changes in comparison with the simple configuration.

An accurate analysis of the separated flow field within the dual chambers with extended ducts by computational fluid dynamics poses a challenge and is beyond the scope of the present work. However, an experimental comparison is provided here in Fig. 10 on the flow performance of the present design relative to two other conventional designs: (1) a prototype three-pass muffler built and studied in Ref. [17], and (2) a current production muffler for a V8 spark-ignition engine. Flow experiments are conducted in a laboratory under ambient conditions to determine the total pressure drop across the elements versus flow rate through them. Note how the pressure drop and therefore flow losses are significantly lower for the present concept in contrast with some of the conventional designs throughout the Reynolds number range of interest.

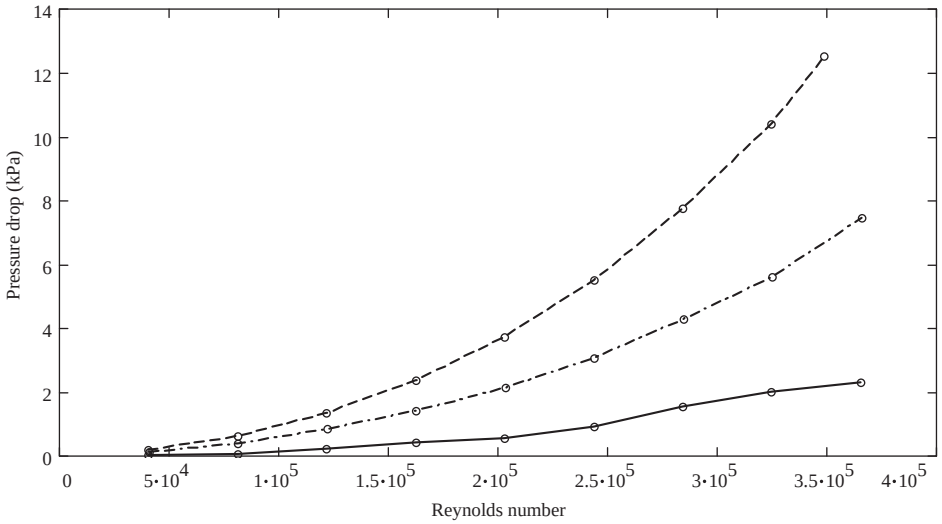

Fig. 10. Pressure drop versus flow rate: ——, dual-chamber muffler; – – –, prototype muffler; – – – –, production muffler.

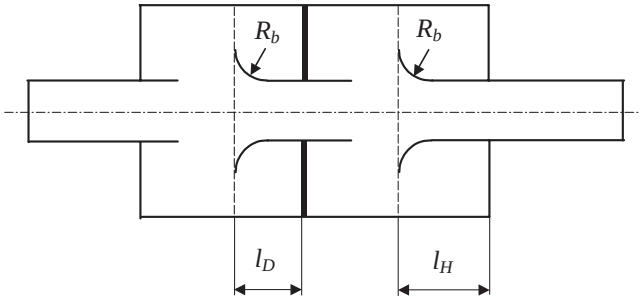

Fig. 11. Dual-chamber muffler with bellmouthed extensions.

The foregoing relatively lower losses can be further reduced by introducing bellmouthed entries into two sharp inlets, as shown in Fig. 11. The effect of curved inlets on the acoustic attenuation is illustrated in Fig. 12 by comparing the FEM solution for the dual chamber of geometry 1 with bellmouthed ducts to that of analytical solution with straight ducts. The specific dimensions are $l_B = l_F = 0.059\,\text{m}$, $l_D = l_H = 0.020\,\text{m}$ and $R_b = 0.4R_2$ with bellmouthed ducts, $l_B = l_F = 0.059\,\text{m}$ and $l_D = l_H = 0.025\,\text{m}$ with straight ducts. The acoustic differences between the two configurations are small, supporting the potential use of curved entrances for further flow improvements, while no flow experiment was conducted with bellmouthed entries.

4. Conclusions

The mode-matching technique has been applied to predict the acoustic behavior of concentric circular dual-chamber mufflers. Comparisons with FEM predictions and experimental results are

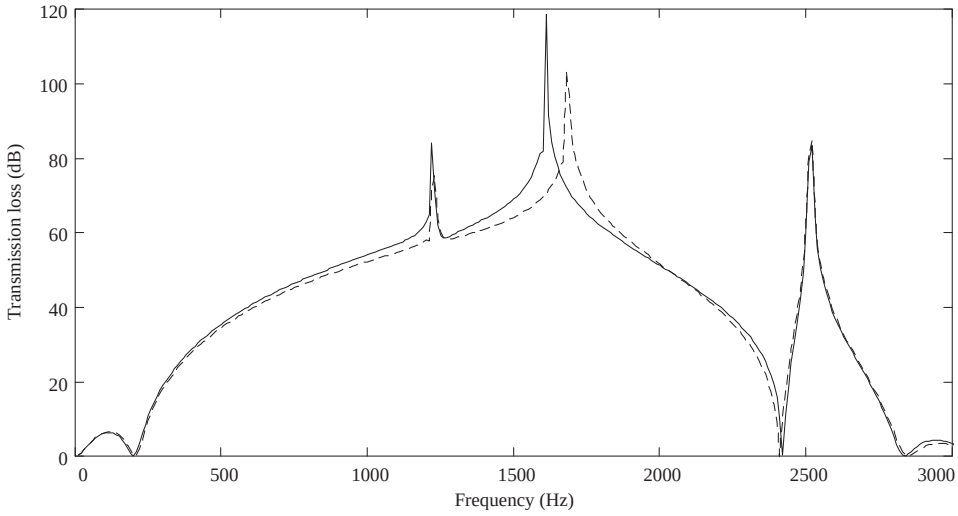

Fig. 12. Transmission loss of dual-chamber muffler with extensions, geometry 1: – – –, bellmouthed, FEM; ——, straight, analytical.

also provided, which are consistent with the analytical approach. Several effects have been studied, including the presence of a baffle inside the muffler, the baffle hole radius, the axial location of the baffle and the extension of the inlet/outlet and baffle ducts. The presence of a centered baffle leads to an acoustic attenuation that exhibits pairs of domes. The first dome of each pair is smaller in amplitude and frequency bandwidth than the second one. As the frequency increases, the first dome of the pair gradually disappears and for the second dome, the frequency bandwidth and amplitude increase, yielding an improved attenuation behavior in comparison with that of the simple expansion chamber. The generation of evanescent higher order modes at the partition leads to an inaccurate prediction of the acoustic performance, even at low frequencies, if the plane wave model is used without end corrections. When the baffle hole radius is reduced, the amplitude and frequency bandwidth of the second dome of each pair become larger. By axially moving the baffle, it is also possible to eliminate some undesirable pass-bands and improve the acoustic behavior. Finally, the use of proper extended ducts can lead to a general increase in the attenuation of the chamber, with amplitudes reaching twice those obtained with a simple expansion chamber. However, a deterioration is observed at low frequencies due to the presence of the baffle, which may be improved, for example, by a Helmholtz resonator. Through FEM predictions, bellmouthed entries have been shown not to hinder the acoustic performance, thereby lending support to the potential use of such flow improvement modifications.

Acknowledgements

This work has been partially supported by Ministerio de Ciencia y Tecnología by means of project DPI2000-0743-C02-01.

Appendix A. Integration of the eigenfunctions

The integrals regarding eigenfunctions (29) and (30) can be evaluated after consideration of the properties of the Bessel functions [18]. The following expressions are used:

$$\langle \psi_{E,s}\psi_{E,s} \rangle_{S_E} = R_2^2 \mathrm{J}_0^2(\alpha_s), \quad \langle \psi_{G,s}\psi_{G,s} \rangle_{S_G} = R_C^2 \mathrm{J}_0^2(\alpha_s), \tag{A.1, A.2}$$

$$\langle \psi_{G,n}\psi_{E,s} \rangle_{S_E} = \begin{cases} \dfrac{2\alpha_n \dfrac{R_2}{R_C}\mathrm{J}_0(\alpha_s)\mathrm{J}_1\left(\alpha_n \dfrac{R_2}{R_C}\right)}{\left(\dfrac{\alpha_n}{R_C}\right)^2 - \left(\dfrac{\alpha_s}{R_2}\right)^2}, & \dfrac{\alpha_n}{R_C} \neq \dfrac{\alpha_s}{R_2}, \\ R_2^2 \mathrm{J}_0^2(\alpha_s), & \dfrac{\alpha_n}{R_C} = \dfrac{\alpha_s}{R_2}, \end{cases} \tag{A.3}$$

$$\langle \psi_{G,n}\psi_{F,s} \rangle_{S_F} = \begin{cases} \dfrac{2\alpha_n \dfrac{R_2}{R_C}\mathrm{J}_1\left(\alpha_n \dfrac{R_2}{R_C}\right)\psi_{F,s}(R_2)}{\left(\dfrac{\beta_{F,s}}{R_C}\right)^2 - \left(\dfrac{\alpha_n}{R_C}\right)^2}, & \alpha_n \neq \beta_{F,s}, \\ R_C^2 \psi_{G,n}(R_C)\psi_{F,s}(R_C) - R_2^2 \psi_{G,n}(R_2)\psi_{F,s}(R_2), & \alpha_n = \beta_{F,s}. \end{cases} \tag{A.4}$$

The information given in Appendix A of Ref. [10] can also be used, with slight modifications that take into account the different radii R_1, R_2 and R_3 considered in the present work.

Appendix B. Plane wave model

The planar wave propagation model is used in order to evaluate its applicability limits and to assess the need for end corrections. While a brief description of the relevant relationships is given in this appendix, the reader is referred to Ref. [1] for a detailed treatment. First, the four-pole matrices of the ducts are obtained. The product of these then yields the four-pole matrix of the entire configuration, which relates the pressure and mass velocity at the inlet and outlet and enables the evaluation of the acoustic attenuation performance by TL. The four-pole matrices of the ducts A, E and I are, respectively,

$$M_A = \begin{bmatrix} \cos(kl_A) & \mathrm{j}Y_A \sin(kl_A) \\ \dfrac{\mathrm{j}}{Y_A}\sin(kl_A) & \cos(kl_A) \end{bmatrix}, \quad M_E = \begin{bmatrix} \cos(kl_E) & \mathrm{j}Y_E \sin(kl_E) \\ \dfrac{\mathrm{j}}{Y_E}\sin(kl_E) & \cos(kl_E) \end{bmatrix},$$

$$M_I = \begin{bmatrix} \cos(kl_I) & \mathrm{j}Y_I \sin(kl_I) \\ \dfrac{\mathrm{j}}{Y_I}\sin(kl_I) & \cos(kl_I) \end{bmatrix}, \tag{B.1–B.3}$$

where $Y_A = c_0/S_A$, $S_A = \pi R_1^2$, $Y_E = c_0/S_E$, $S_E = \pi R_2^2$, $Y_I = c_0/S_I$ and $S_I = \pi R_3^2$. For the four-pole matrices of the two chambers C and G,

$$M_C = \begin{bmatrix} \cos(kl_C) & \mathrm{j}Y_C \sin(kl_C) \\ \dfrac{\mathrm{j}}{Y_C}\sin(kl_C) & \cos(kl_C) \end{bmatrix}, \quad M_G = \begin{bmatrix} \cos(kl_G) & \mathrm{j}Y_G \sin(kl_G) \\ \dfrac{\mathrm{j}}{Y_G}\sin(kl_G) & \cos(kl_G) \end{bmatrix}, \tag{B.4, B.5}$$

where $Y_C = c_0/S_C$, $S_C = \pi R_C^2$, $Y_G = c_0/S_G$ and $S_G = \pi R_C^2$. Finally, the four extended regions are described by

$$M_B = \begin{bmatrix} 1 & 0 \\ \dfrac{1}{-\mathrm{j}Y_B \cot(kl_B)} & 1 \end{bmatrix}, \quad M_D = \begin{bmatrix} 1 & 0 \\ \dfrac{1}{-\mathrm{j}Y_D \cot(kl_D)} & 1 \end{bmatrix},$$
$$M_F = \begin{bmatrix} 1 & 0 \\ \dfrac{1}{-\mathrm{j}Y_F \cot(kl_F)} & 1 \end{bmatrix}, \quad M_H = \begin{bmatrix} 1 & 0 \\ \dfrac{1}{-\mathrm{j}Y_H \cot(kl_H)} & 1 \end{bmatrix} \tag{B.6–B.9}$$

with $Y_B = c_0/S_B$, $S_B = \pi(R_C^2 - R_1^2)$, $Y_D = c_0/S_D$, $S_D = \pi(R_C^2 - R_2^2)$, $Y_F = c_0/S_F$, $S_F = \pi(R_C^2 - R_2^2)$, $Y_H = c_0/S_H$ and $S_H = \pi(R_C^2 - R_3^2)$. The matrix of the entire configuration relates the pressure P and mass velocity V at the inlet and outlet by

$$\begin{bmatrix} P_{inlet} \\ V_{inlet} \end{bmatrix} = \begin{bmatrix} T_{11} & T_{12} \\ T_{21} & T_{22} \end{bmatrix} \begin{bmatrix} P_{outlet} \\ V_{outlet} \end{bmatrix}, \tag{B.10}$$

where T_{11}, T_{12}, T_{21} and T_{22} are referred to as the four poles of the acoustical system, which are obtained by multiplying the previous matrices as

$$\begin{bmatrix} T_{11} & T_{12} \\ T_{21} & T_{22} \end{bmatrix} = M_A M_B M_C M_D M_E M_F M_G M_H M_I. \tag{B.11}$$

Finally, the transmission loss is obtained by [1]

$$TL = 20 \log \left[\left(\frac{Y_I}{Y_A} \right)^{1/2} \left| \frac{T_{11} + T_{12}/Y_I + T_{21} Y_A + T_{22}(Y_A/Y_I)}{2} \right| \right]. \tag{B.12}$$

In order to improve the results of the plane wave model, end corrections can be used for the area changes (two expansions and two contractions). For the inlet and outlet ducts with no extension, the values given by Eqs. (32) and (33) can be used as extended lengths l_B and l_H, respectively. If extended ducts are included in the chamber, the results of Ref. [2] can be applied to correct the plane wave model (this is not considered in the present work). For a baffle with no extension ($l_D = l_F = 0$), the application of the foregoing approximate corrections is not suitable due to baffle's small thickness in comparison with the radius. To improve the accuracy, finite element calculations have been performed here to obtain the 1-D model corrections for the baffle following the procedure described in Ref. [15]. The computational domain considered and the 1-D end correction δ_{baffle} associated with the baffle hole are shown in Fig. A.1, and the numerical results are given in Table A.1 (by means of a polynomial fit). The lengths l_D and l_F, which are initially zero, can then use the values indicated in Table A.1 (see Figs. 2 and 3, and Fig. 6). Since the lengths l_{T1} and l_{T2} are kept constant for a given configuration, these end corrections reduce l_C and l_G slightly.

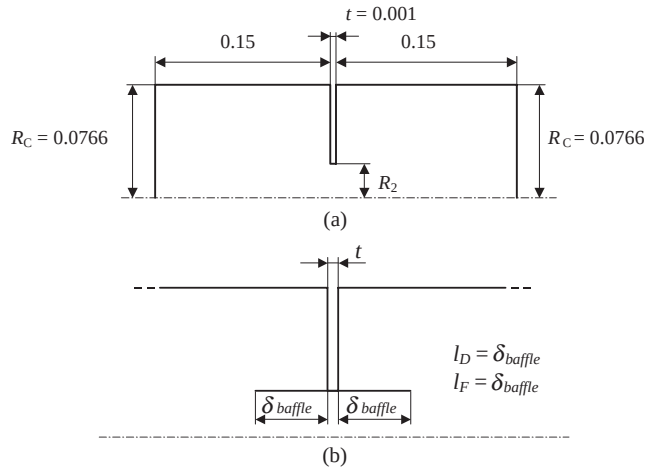

Fig. A.1. (a) Axisymmetric finite element domain for the evaluation of end corrections (dimensions in m) and (b) extensions of the corrected plane wave model in the baffle.

Table A.1
End correction δ_{baffle} for the baffle hole

R_2 (m)	δ_{baffle}
0.0125	$R_2(0.61237 + 0.075377\ kR_2 + 0.383753(kR_2)^2 - 0.283319(kR_2)^3)$
0.0175	$R_2(0.539896 + 0.065188\ kR_2 + 0.11981(kR_2)^2 + 0.079608(kR_2)^3)$
0.0243	$R_2(0.44544 + 0.049955kR_2 + 0.022517(kR_2)^2 + 0.083479(kR_2)^3)$
0.0325	$R_2(0.338898 + 0.03158kR_2 + 0.001504(kR_2)^2 + 0.038375(kR_2)^3)$

Appendix C. Nomenclature

$A_n, B_n, C_n, D_n, E_n, F_n, G_n, H_n, I_n$	propagation coefficients in regions $A, B, C, D, E, F, G, H, I$ (see Fig. 1)
J_0, J_1	Bessel functions of the first kind and order 0 and 1
k	wave number
$k_{A,n}$	$= [k^2 - (\alpha_n/R_1)^2]^{1/2}$, axial wave number in region A
$k_{B,n}$	$= [k^2 - (\beta_{B,n}/R_C)^2]^{1/2}$, axial wave number in region B
$k_{E,n}$	$= [k^2 - (\alpha_n/R_2)^2]^{1/2}$, axial wave number in region E
$k_{F,n}$	$= [k^2 - (\beta_{F,n}/R_C)^2]^{1/2}$, axial wave number in region F
$k_{H,n}$	$= [k^2 - (\beta_{H,n}/R_C)^2]^{1/2}$, axial wave number in region H
$l_B, l_C, l_D, l_E, l_F, l_G, l_H$	lengths of regions B, C, D, E, F, G, H
$M_A, M_B, M_C, M_D, M_E, M_F, M_G, M_H, M_I$	four pole matrices of regions $A, B, C, D, E, F, G, H, I$
n	mode number
P	acoustic pressure
R_1, R_2, R_3, R_C, R_b	radii of inlet duct, baffle hole, outlet duct, chamber and bellmouth

s	orthogonal expansion terms
$S_A, S_B, S_C, S_D, S_E, S_F, S_G, S_H, S_I$	cross-sectional areas of regions $A, B, C, D, E, F, G, H, I$
t	baffle thickness
$T_{11}, T_{12}, T_{21}, T_{22}$	four pole matrix elements of the acoustic system
U	acoustic velocity
V	acoustic mass velocity
Y_0, Y_1	Bessel functions of the second kind and order 0 and 1
$Y_A, Y_B, Y_C, Y_D, Y_E, Y_F, Y_G, Y_H, Y_I$	characteristic impedance of regions $A, B, C, D, E, F, G, H, I$
α_n	zeros of $J_1(\alpha_n) = 0$ (hollow ducts A, C, E, G, I)
$\beta_{B,n}$	zeros of $J_1(\beta_{B,n}R_1/R_C) - [J_1(\beta_{B,n})/Y_1(\beta_{B,n})]Y_1(\beta_{B,n}R_1/R_C) = 0$ (annular duct B)
$\beta_{F,n}$	zeros of $J_1(\beta_{F,n}R_2/R_C) - [J_1(\beta_{F,n})/Y_1/(\beta_{F,n})]Y_1(\beta_{F,n}R_2/R_C) = 0$ (annular duct F)
$\beta_{H,n}$	zeros of $J_1(\beta_{H,n}R_3/R_C) - [J_1(\beta_{H,n})/Y_1/(\beta_{H,n})]Y_1(\beta_{H,n}R_3/R_C) = 0$ (annular duct H)
$\delta_{inlet}, \delta_{outlet}, \delta_{baffle}$	end corrections for the inlet/outlet ducts and the baffle hole
$\psi_{A,n}(r)$	$= J_0(\alpha_n r/R_1)$, for region A
$\psi_{B,n}(r)$	$= J_0(\beta_{B,n}r/R_C) - [J_1(\beta_{B,n})/Y_1(\beta_{B,n})]Y_0(\beta_{B,n}r/R_C)$, for region B
$\psi_{E,n}(r)$	$= J_0(\alpha_n r/R_2)$, for region E
$\psi_{F,n}(r)$	$= J_0(\beta_{F,n}r/R_C) - [J_1(\beta_{F,n})/Y_1(\beta_{F,n})]Y_0(\beta_{F,n}r/R_C)$, for region F
$\psi_{G,n}(r)$	$= J_0(\alpha_n r/R_C)$, for region G

References

[1] M.L. Munjal, Acoustics of Ducts and Mufflers, Wiley-Interscience, New York, 1987.

[2] K.S. Peat, The acoustical impedance at the junction of an extended inlet or outlet duct, Journal of Sound and Vibration 150 (1991) 101–110.

[3] A. Selamet, Z.L. Ji, Acoustic attenuation performance of circular expansion chambers with offset inlet/outlet: I. Analytical approach, Journal of Sound and Vibration 213 (1998) 601–617.

[4] A. Selamet, Z.L. Ji, Acoustic attenuation performance of circular flow-reversing chambers, Journal of the Acoustical Society of America 104 (1998) 2867–2877.

[5] K.L. Chan, S.R. Judah, Mode-matching analysis of a waveguide junction formed by a circular and a larger elliptic waveguide, IEEE Proceedings on Microwave Antennas and Propagation 145 (1998) 123–127.

[6] G. Conciauro, M. Guglielmi, R. Sorrentino, Advanced Modal Analysis, Wiley, Chichester, 2000.

[7] A. Selamet, P.M. Radavich, The effect of length on the acoustic attenuation performance of concentric chambers: an analytical, numerical and experimental investigation, Journal of Sound and Vibration 201 (1997) 407–426.

[8] J.G. Ih, B.H. Lee, Analysis of higher-order mode effects in the circular expansion chamber with mean flow, Journal of the Acoustical Society of America 77 (1985) 1377–1388.

[9] A. Selamet, Z.L. Ji, P.M. Radavich, Acoustic attenuation performance of circular expansion chambers with offset inlet/outlet: II, Comparison with experimental and computational studies, Journal of Sound and Vibration 213 (1998) 619–641.

[10] A. Selamet, Z.L. Ji, Acoustic attenuation performance of circular expansion chambers with extended inlet/outlet, Journal of Sound and Vibration 223 (1999) 197–212.
[11] P. Xiao, M.G. Prasad, Insertion loss studies of a baffle-simple expansion chamber system, Journal of the Acoustical Society of America 97 (1995) 3255.
[12] K.H. Huebner, E.A. Thorton, T.G. Byrom, The Finite Element Method for Engineers, 3rd Edition, Wiley-Interscience, New York, 1995.
[13] A. Selamet, N.S. Dickey, J.M. Novak, The Herschel–Quincke tube: a theoretical, computational, and experimental investigation, Journal of the Acoustical Society of America 96 (1994) 3177–3185.
[14] J. Kergomard, A. Garcia, Simple discontinuities in acoustic waveguides at low frequencies: critical analysis and formulae, Journal of Sound and Vibration 114 (1987) 465–479.
[15] A.D. Sahasrabudhe, M.L. Munjal, S. Anantha Ramu, Analysis of inertance due to higher order mode effects in a sudden area discontinuity, Journal of Sound and Vibration 185 (1995) 515–529.
[16] A. Selamet, Z.L. Ji, Wave reflections from duct terminations, Journal of the Acoustical Society of America 109 (2001) 1304–1311.
[17] N.S. Dickey, A. Selamet, J.M. Novak, Multi-pass perforated tube silencers: a computational approach, Journal of Sound and Vibration 211 (1998) 435–448.
[18] J. Rey, A. Castro, Funciones de Bessel, Dossat, Madrid, 1958.